Research Article

Design and Application of Automatic Control System for Fully Mechanized Mining Face in Coal Mine

Zhi Yuan,[1] **Huanlei Chi,**[2] **and Yan Cao** [2]

[1]*China National Coal Mining Equipment Co., Ltd., Beijing 100011, China*
[2]*China Coal Equipment Research Institute, Beijing 100011, China*

Correspondence should be addressed to Yan Cao; caoyan@chinacoal.com

In order to improve the automatic control effect of fully mechanized mining face in coal mine, this paper combines the literature research method to analyze the disadvantages of traditional research and combines the demand analysis to analyze the structure of the automatic control system of fully mechanized mining face in coal mine. Moreover, this paper uses an improved algorithm to improve the system performance, uses the analytical approximation method to calculate and eliminate the loading phase of the fourth-order input and output equal-length cavity filter and the fourth-order input and output unequal-length cavity filter, and obtain the correct coupling matrix. In addition, this paper uses the genetic algorithm to calculate and eliminate the loading phase of the sixth-order input-output equal-length cavity filter and the sixth-order input-output unequal-length cavity filter. In addition, after the system is constructed, the performance analysis of the system can be known through experimental research. The research results show that the automatic control system of fully mechanized mining face in coal mine proposed in this paper has a good intelligent control effect.

1. Introduction

The design based on programmable logic controller (PLC) greatly improves the maintainability of the system, reduces the difficulty of programming, and takes into account the needs of on-site frequency conversion equipment. Moreover, it can better meet the strategic needs of "mechanized replacement, automated labor reduction" and provide technical support for the safe and efficient production of coal mines, reducing labor and improving efficiency. At the same time, it can effectively improve the system transportation and production efficiency [1, 2].

Through the analysis of the linkage and cooperation between the various agencies during the fully mechanized mining operation of the shearer, and the actual situation of the coal mine and the control requirements of the fully mechanized mining operation of the shearer, the intelligent fully mechanized mining control system needs to mainly include four parts: machinery, drive, control, and correction. When the control system is applied, professional technicians

first analyze the distribution and geological information of the coal seam in the fully mechanized mining face. After that, a reasonable cutting path scheme is set according to the actual situation in the well to meet the needs of automatic cutting and fully mechanized recovery. After the plan is determined, the controller manually controls the cutting mechanism to perform the cutting operation under manual control. At this time, the intelligent fully mechanized mining operation control system records the cutting path and position coordinates of the shearer under manual control for subsequent automatic cutting control [3]. After entering the control information, the system corrects the path information of the shearer according to the preset correction scheme, and realizes the intelligent control of the fully mechanized mining operation of the shearer through the cutting drum and the feed speed of the shearer [4]. The control system does not rely on the memory cutting operation, but realizes more the optimization of the feed speed and the cutting speed under the premise of the cutting operation according to the memory cutting path through the

comprehensive monitoring of the cutting speed and the feeding speed of the shearer. Moreover, it meets the requirements of high efficiency and economy of shearer cutting operations under various working conditions, and enhances the adaptability of the intelligent fully mechanized mining control system to the complex underground environment of coal mines [5].

In the mining process of the fully mechanized mining face, the monitoring center inside the coal mine roadway is equipped with an intrinsically safe control platform. Real-time monitoring and performance testing of the entire mining equipment are carried out at the same time [6]. Two different serial interfaces are provided in the shearer equipment, and the corresponding remote control protocol is provided by using the automatic control system, and the relevant parameters in the monitoring work are directly transmitted to the terminal system for effective control. In this way, the real-time reception of shearer data and related transmission work can be brought into full play. During the construction, the control mode of the terminal system can effectively realize the two-way information communication to the control mode. In order to effectively cooperate and coordinate, the remote control of the entire coal mining face is finally realized, which improves the working efficiency and stability of the entire shearer [7].

In the mining process of a fully mechanized mining face, effective inspection is required. During the working process of emulsion pump and spray pump, the pressure in the outlet area and the internal flow rate are effectively controlled, focusing on controlling the liquid position inside the emulsion. The height, the oil level of the fuel tank, and the automatic replenishment of the emulsion water, etc., realize the real-time control of the emulsion concentration, and realize the automatic proportioning of various materials [8]. During the work, it is necessary to record the key working parameters of the emulsion pump and the spray pump in real time, and directly transmit them to the terminal system for processing through the collection of key parameters, and perform dynamic simulation and parameterization in the central control system. Display of the curve has to be carried out. The corresponding sensor equipment needs to be equipped inside the pumping station. The sensors and monitoring equipment must work in coordination with each other and meet the working requirements of the coal mining face. There must be a corresponding interface between the central control equipment and the Internet communication interface. Information channel at the pumping station has a unique automatic control system. Through the effective connection between the reserved controller and the terminal system, the real-time information response of the internal automatic control system of the pumping station is effectively realized. The automatic control of the motor has a good working effect, and it also truly realizes the two-way control function between the emulsion pump and the jet pump, which can effectively ensure the real-time start and stop of the equipment [9].

The key to controlling the automatic shearer is to ensure that the cutting height of the shearer drum is automatically adjusted according to the changing coal seam. Only when the intelligent shearer can effectively identify the thickness of the coal seam roof and the interface between the coal seam and the rock layer can the automatic shearer be controlled. At present, memory technology is widely used in coal mining field to identify coal seams and rock formations [10]. Memory shearer control cutting process has the following stages: ① Memory path cutting and processing data. It mainly processes the memory and collection of path cutting data. ② Automatic increase. When the shearer is working, the path that has been memorized provides the shearer with a standard for cutting and walking. When the shearer encounters changes in the geological coal seam, there will be a big difference between the actual and memory parameters. The shearer can automatically adjust its height according to memory and artificial immunity [11]. When the coal seam undergoes very large geological changes and the drum cannot automatically adjust the height, the intelligent shearer can realize remote operation control, manually correct the running trajectory, and memorize it. When the same situation occurs again, the device will automatically adjust based on memory. The cutting memory principle of the intelligent shearer is that manual operation is required when working for the first time, and the self-energy shearer will automatically memorize various parameters such as position and path. During the work, these memories are regular memory points. When the coal seam changes in the working process of the shearer, the equipment needs to be controlled manually. The change point at this time is the key point. The intelligent shearer will memorize the key point, and the automatic control of the intelligent shearer will be based on the conventional memory point. The method combined with key memory points improves the accuracy of its control [12].

In the current information age, the software and hardware systems in the automation control system of underground electrical equipment are also developing toward a higher level of automation control based on advanced information technology and computer technology. The corresponding equipment system and software and hardware systems are optimized [13]. Since the content of downhole operations is complex and the operating environment is harsh, this environment will have a direct impact on the efficiency of downhole operations and production costs [14]. When selecting PLC equipment, it is necessary to select the scale and performance parameters of PLC equipment based on the fine electrical equipment and its automation control requirements, its own operating status and functional requirements, combined with the actual operation of the system. For example, the application of micro PLC equipment in the downhole protection system requires real-time monitoring of downhole gas concentration without controlling other environmental factors [15]. The application of this kind of PLC equipment helps to reduce the equipment procurement cost and daily operating energy consumption, while meeting the requirements of equipment performance, production, and economy. In the drainage control system, since the real-time water level will affect its working state, and various indicators will limit the size of the mine water output and drainage efficiency, in the
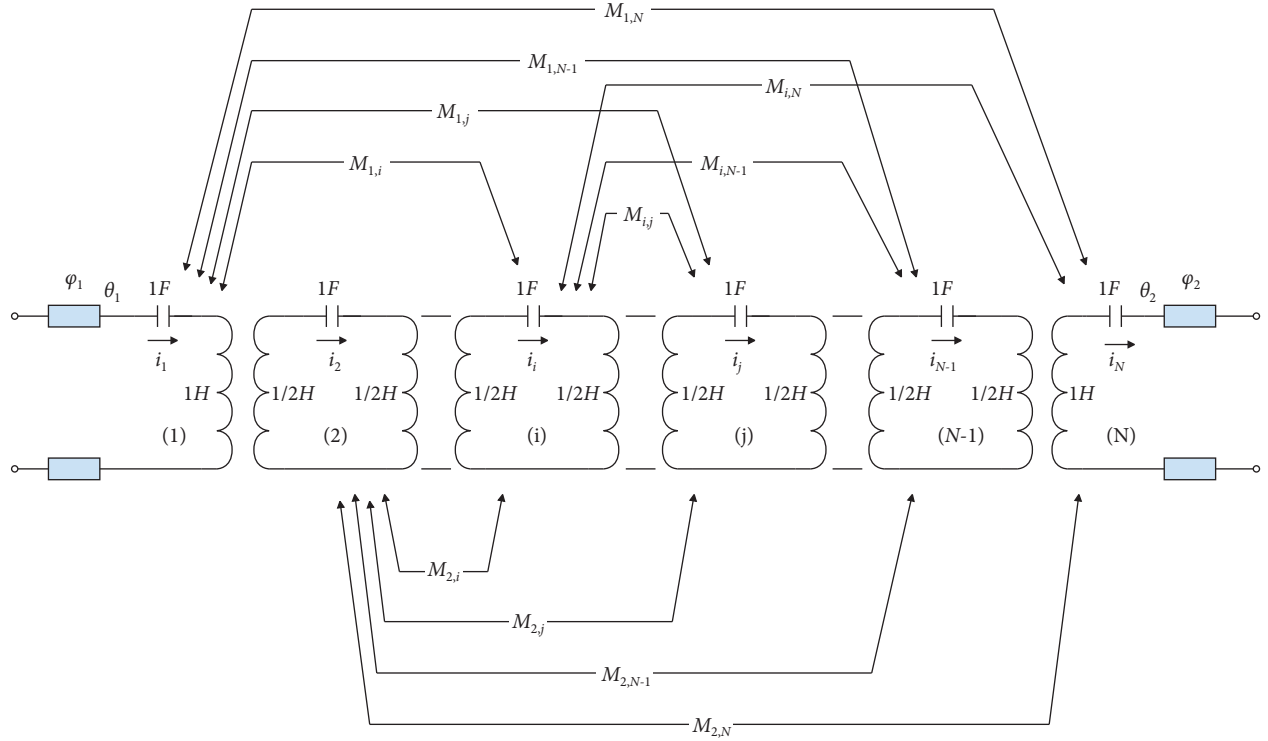
Figure 1: Equivalent circuit model of a cross-coupled filter with loaded phases.

face of a relatively large amount of automatic control calculation and high real-time requirements, the mentioned micro PLC equipment cannot meet the requirements, and large-scale PLC equipment with more powerful computing power and higher performance needs to be selected to meet the requirements [16].

It can be seen from the research that some systems can only use the communication of the system to diagnose the status of the system, and cannot give an accurate location to the collective fault point. The system cannot forecast, warn, and provide users with countermeasures and plans to avoid accidents, and the system cannot provide an effective basis for the causes of accidents.

In view of this, it has become the most basic and urgent requirement of current coal mine production to develop a coal mine underground comprehensive automation system device with good real-time performance, high stability, and strong anti-interference ability, and to realize the automatic control of large-scale equipment in the working face.

This paper analyzes the automatic control and performance of the fully mechanized mining face in the coal mine, and builds an intelligent control system to improve the automatic control effect of the fully mechanized mining face in the coal mine.

2. Filter Control of Fully Mechanized Mining Face in Coal Mine

2.1. Phase Loading Elimination. Before filter tuning, the phase loading of the network model parameters needs to be eliminated. Phase loading has an effect on the extreme value

of the admittance parameter $[Y]$ and the location of the pole. If the influence of phase loading cannot be eliminated correctly, the correct coupling matrix cannot be obtained, and it is difficult to debug the filter into the specification during the debugging process. The phase loading effect is the phase difference between the measured and ideal values of the response. There are three main factors leading to the phase loading effect. That is, (1) the one caused by the difference between the ideal circuit model and the reference plane of the actual circuit model, (2) the distribution effect of the input and output coupling elements, and (3) the length of the transmission line additionally introduced during the measurement. Figure 1 shows the equivalent circuit model of the cross-coupled filter including the loaded phase.

According to the classical filter synthesis theory, the reflection parameter S11 rational polynomial of the n-order low-pass filter can be expressed as [17]:

$$S_{11} = \frac{F(s)/\varepsilon_R}{E(s)}. \tag{1}$$

In the formula: $E(s)$ is the nth order polynomial with coefficient $e_0, e_1, e_2 \ldots e_n$, $F(s)$ is the nth order polynomial with coefficient $f_0, f_1, f_2 \ldots f_n$, and Ω is the value that determines the normalization of the highest order coefficients of $E(s)$ and $F(s)$. We assume that there is $s = j\Omega$ and Ω is the normalized frequency in the low-pass band, and the phase of the scattering parameter can be expressed as formula (2):

$$\phi S_{11}(\Omega) = \tan^{-1}\frac{e_{(n-1)}\Omega^{n-1} + e_{(n-2)}\Omega^{n-2} + \ldots + e_{0,i}}{\Omega^n + e_{(n-1),i}\Omega^{n-1} + \ldots + e_{0,r}}. \tag{2}$$

Because coefficient $f_0, f_1, f_2 \ldots f_n$ is pure real or pure imaginary, when there is $s = j\Omega$, $F(s)$ is a function that gets real. The phase of the reflection parameter S is independent of the coefficients of the polynomial $F(s)$. When there is $\Omega \longrightarrow +\infty$, there is [18]:

$$\phi S_{11} \approx \frac{a_1}{\Omega}. \tag{3}$$

For the narrowband filter real frequency ω far away from the passband frequency domain, the asymptotic response of the filter group delay can be expressed as:

$$\tau S_{11} = \frac{\partial \phi \ S_{11}}{\partial \omega} \approx \frac{a}{\Omega^2}. \tag{4}$$

The phase loading is due to higher-order modes near the coupling elements of the input and output ports, and its circuit model can be represented by a reactive T-network connected to the phase offset φ. The network is over a wide frequency range and the phase offset can be approximated as a function of:

$$\varphi = \varphi_0 + \beta \Delta l. \tag{5}$$

In the formula: φ_0 is a constant term, which is called the loading phase and which does not change with frequency. β is the interface line propagation constant and Δl is the equivalent length of the transmission line to be embedded.

In the filter physical model, there is always an unwanted transmission line length at the filter port between the physical reference plane and the corresponding transformer port in the circuit model. The length of this transmission line is difficult to measure due to the presence of higher-order modal effects at the ports of the physical filter model.

For a typical transmission line, the propagation constant β can be approximated as: when there is $k \gg k_c$, there is

$$\beta \approx k - \frac{k_c^2}{2k}. \tag{6}$$

When there is $k \gg k_c$, $k_c^2/2k$ tends to a small constant, and the propagation constant β can be further approximated as

$$\beta \longrightarrow \omega\sqrt{\mu\varepsilon} - b. \tag{7}$$

The coefficient of the first term in formula (7) is a known constant related to the dielectric constant of the transmission line, and b is a very small constant that has no effect on the method. It can be seen from formula (4) that when the operating frequency is much higher than the cutoff frequency, the reflection parameter S_{11} group delay of the physical filter model assuming the length of the transmission line can be expressed as:

$$\tau S_{11} = -\frac{a_2}{\Omega^2} - 2\sqrt{\mu\varepsilon}\Delta l. \tag{8}$$

Δl is the length of the removed transmission line. It can be seen from formula (8) that the length of the transmission line results in a constant shift in the group delay. The constant displacement can be determined by curve-fitting the physical model group delay at frequencies far below or above the center frequency in the functional form of formula (8). After the parametric centroid is found, the following phase changes are removed from the measured phase [19]:

$$\Delta\varphi S_{11} = -2\beta\Delta l \approx -2\Delta l\sqrt{\mu\varepsilon}\omega. \tag{9}$$

The constant term in formula (8) can be obtained by least squares fitting.

The input and output ports of the fourth-order cross-coupling filter are of equal length. The center frequency is $f_0 = 2.069$ GHz, the bandwidth is Bw = 110MIEz, the return loss is RL = 20 dB, and the finite transmission zero point $\pm 2j$ is normalized.

Figure 2 is the top view and side view of the full cavity model established in HFSS (high-frequency structure simulator), the equal lengths of the input and output ports are both 10 mm. The phase shift load of the input port to remove the phase load is $\varphi_1 = 04.55$ degrees, and the transmission line length $\Delta l_1 = 0.7331$ mm. At the same time, the phase shift load of the output port is $\varphi_2 = 104.57$ degrees, and the electrical length of the output port is $\Delta l_2 = 0.5971$ mm. The phase shift loads of the two ports are compared, and it can be seen that the two are approximately equal.

Figure 3(a) is the phase diagram of S_{11} removal of loading, the black solid line in the figure does not remove the phase loading of the scattering parameters, and the red dotted line is the scattering parameters after removing the phase loading. Figure 3(b) is a diagram of S_{21} removing the phase loading. The black solid line in the figure does not remove the phase loading for scattering parameters, and the red dotted line is S_{21} after removing the phase loading. It can be seen from the figure that the two lines are quite different in the interval [−6,6], and the difference in the figure shows the effect of phase loading on the scattering parameters. If it cannot be eliminated correctly, the correct coupling matrix cannot be obtained. Figure 3 illustrates the asymptotic properties of the phase of the scattering parameters S_{11} and S_{21} of the physical model after removing the phase load.

The input and output ports of the fourth-order cross-coupling filter are not of equal length. The center frequency is $f_0 = 2.069$ GHz, the bandwidth is Bw = 110MIHz, the return loss is RL = 20 dB, and the finite transmission zero point $\pm 2j$ is normalized.

2.2. Genetic Algorithm to Eliminate Loading Phase.

In a lossless filter network that extracts the scattering parameter S, there are no transmission lines at the input and output ports of the filter network. However, in practice, a transmission line will be introduced at the input and output ports when the parameters are extracted, and the introduced transmission line will change the reference surface of the scattering parameters. The phase shift of the scattering parameter S caused by the transmission line is
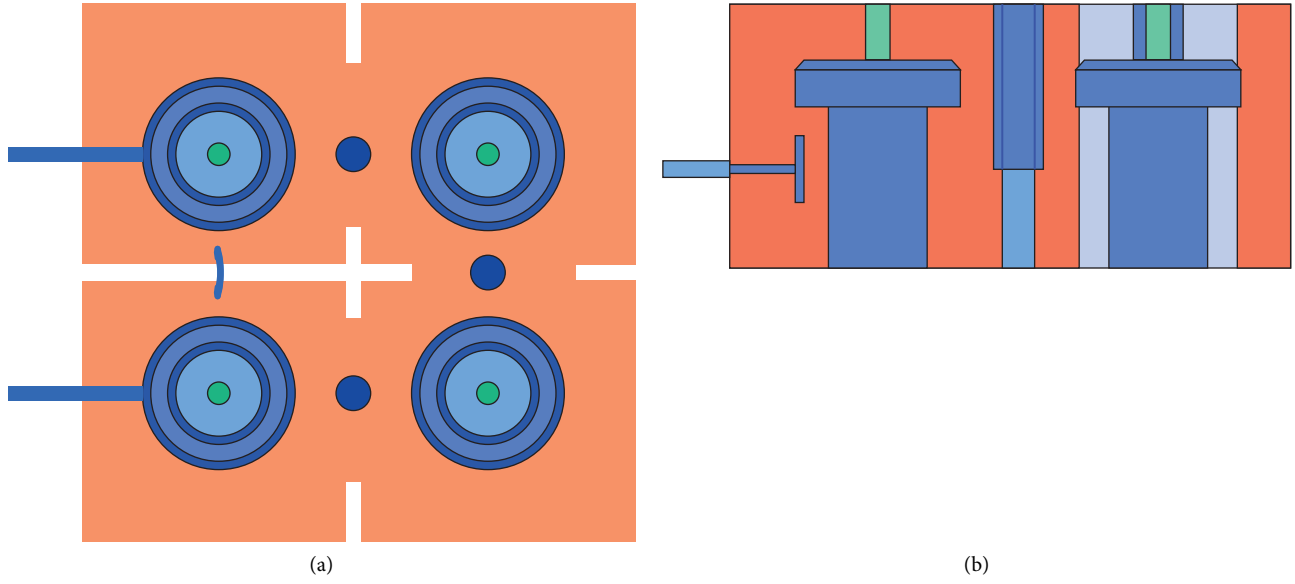
$$\varphi = \varphi_0 + \beta\Delta l. \tag{10}$$

(a)

(b)

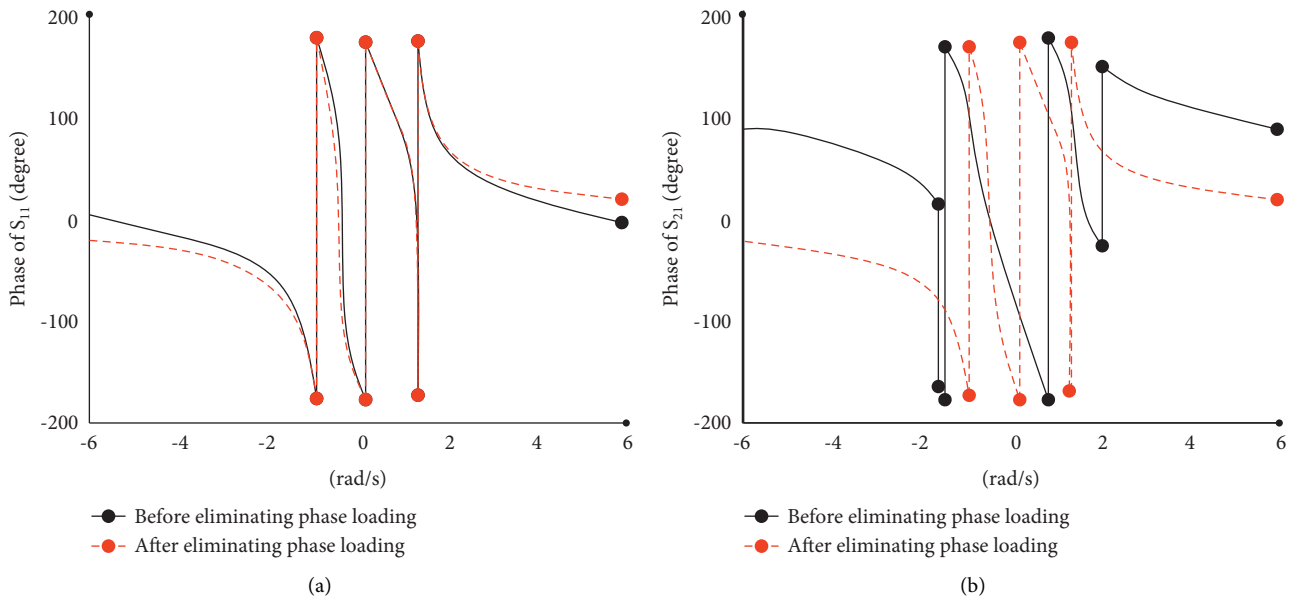FIGURE 2: Full cavity model. (a) Top view. (b) Side view.

(a)

(b)

FIGURE 3: Comparison diagram after removing the loading phase. (a) Comparison before and after removing the loading phase S_{11}. (b) Comparison before and after removing the loading phase S_{21}.

In the formula, φ_0 is the loading phase at the input/output port, f_0 is the center frequency of the filter, and the electrical length of the transmission line at the $\beta\Delta l$ port at frequency f_0 is

$$\beta\Delta l = \frac{f\theta_0}{f_0}. \tag{11}$$

Formula (11) is substituted into formula (10):

$$\varphi = \varphi_0 + \frac{f\theta_0}{f_0}. \tag{12}$$

The phase shift of the scattering parameter S can be removed by the following formula:

$$\begin{aligned}
S_{11} &= S_{11}^{\text{mea}} \exp\left(2i\varphi_1\right), \\
S_{21} &= S_{21}^{\text{mea}} \exp\left[i\left(\varphi_1 + \varphi_2\right)\right].
\end{aligned} \tag{13}$$

In the formula, there is $\varphi_1 = \varphi_2$. S_{11}^{mea} and S_{21}^{mea} are the scattering parameters extracted by software simulation, and S_{11} and S_{21} are the scattering parameters after eliminating the phase loading. The characteristic polyphase formula of the scattering parameters after removing the phase shift is
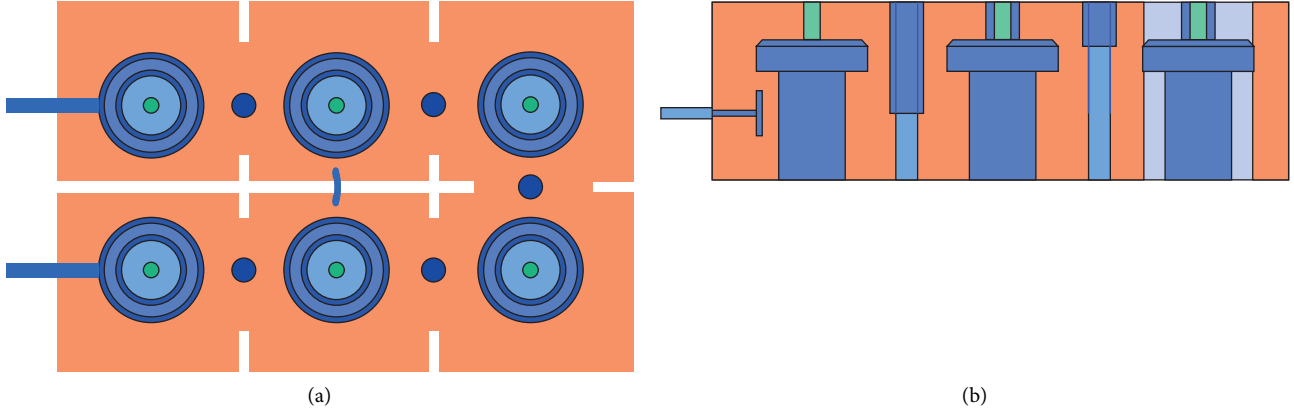
(a)

(b)

Figure 4: Top view and side view of sixth-order cross-coupling filter. (a) Top view. (b) Side view.

$$S_{11}(s) = \frac{F(s)}{E(s)} = \frac{\sum_{k=0}^{n} a_{1k} s^k}{\sum_{k=0}^{n} b_k s^k},$$

$$S_{21}(s) = \frac{P(s)}{E(s)} = \frac{\sum_{k=0}^{n_z} a_{2k} s^k}{\sum_{k=0}^{n} b_k s^k}. \tag{14}$$

In the formula, s is the normalized complex frequency domain, n is the order of the filter, and n_z is the number of finite transmission zeros of the filter. Meanwhile, a_{1k}, a_{2k}, and b_k are the coefficients of the characteristic polynomials $F(s)$, $P(s)$, and $E(s)$, respectively, and N_s is the number of sampling frequency points. Formula (14) can be rewritten as a matrix equation:

$$\begin{bmatrix} V_n & 0_{N_s \times (n+1)} - S_{11} V_n \\ 0_{N_s \times (n+1)} & V_{n_z} - S_{21} V_n \end{bmatrix} \times \begin{bmatrix} a_1 \\ a_2 \\ b \end{bmatrix} = M \times \begin{bmatrix} a_1 \\ a_2 \\ b \end{bmatrix} = 0. \tag{15}$$

In the formula, there is $a_1 = [a_{10}, a_{11}, \ldots, a_{1n}]$, $a_2 = [a_{20}, a_{21}, \ldots, a_{2n}]$, $b = [b_0, b_1, \ldots, b_n]$. Meanwhile, there is $S_{11} = \text{diag}\{S_{11}(s_i)\}$, $S_{21} = \text{diag}\{S_{21}(s_i)\}$. V_n is an n-order Vandermonde matrix, and there is $M = \begin{bmatrix} V_n & 0_{N_s \times (n+1)} - S_{11} V_n \\ 0_{N_s \times (n+1)} & V_{n_z} - S_{21} V_n \end{bmatrix}$.

The unknown parameters can be obtained by genetic algorithm, and the objective function is

$$\text{costfum} = \sum_{i=1}^{N_S} \left[\left(\left[\left| S_{21}^{\text{ext}}(s_i) \right| \right] - \left| S_{21}^{\text{mea}}(s_i) \right| \right)^2 \right. \tag{16}$$
$$\left. + \left(\left[\left| S_{11}^{\text{ext}}(s_i) \right| \right] - \left| S_{11}^{\text{mea}}(s_i) \right| \right)^2 \right].$$

In the formula, $S_{11}^{\text{mea}}(s_i)$ and $S_{21}^{\text{mea}}(s_i)$ are the sampling points of the simulated scattering parameters, and $S_{11}^{\text{ext}}(s_i)$ and $S_{21}^{\text{ext}}(s_i)$ are the values of the extracted scattering parameters at the sampling frequency point.

The sixth-order cross-coupling filter with equal length of the port is input and output, the center frequency is $f_0 = 2.069$ GH, the bandwidth is Bw = 110 MIz, the return loss is RL = 20 dB, and the finite transmission zero point $\pm 2j$ is normalized.

Figure 4 is a top view and a side view of the sixth-order cross-coupling filter, and the input and output ports are equal in length at 10 mm. The genetic algorithm is used to eliminate the loading phase, and the load phases of the input and output ports are obtained as $\varphi_1 = 103.35$ degrees, $\varphi_2 = 103.36$ degrees, and the load difference between the two ports is 0.01. Therefore, the load of the two ports can be approximately equal. The transmission line lengths of the input and output ports are $\Delta l_1 = 0.5579$ mm and $\Delta l_2 = 0.6158$ mm, respectively. Figure 5(a) is the phase diagram of S_{11} removal of loading, the black solid line in the figure is the unloaded phase without the scattering parameters, and the red dotted line is the scattering parameters after removing the loading phase. Figure 5(b) is the phase diagram of S_{21} removal of loading, the black solid line in the figure does not remove the loading phase for the scattering parameters, and the red dotted line is the scattering parameters after removing the loading phase. It can be seen from Figure 4 that there is a large difference before and after data processing, which indicates that the loading phase has a great influence on the scattering parameters and the necessity of eliminating the loading phase.

It can be seen from Figure 4 that the input and output ports are not of equal length, the length of the input port is 10 mm, and the length of the output port is 13 mm. The length of the port is different, and the scattering parameters extracted from the filter are also different. The genetic algorithm is used to eliminate the loading phase, and the loading phases of the input and output ports are obtained as $\varphi_1 = 1038$ degrees and $\varphi_2 = 118.12$ degrees, respectively. The length ratio of the output to the input port is 1.3 : 1, the load phase ratio is $\varphi_2 / \varphi_1 = 1.14$, the difference between the two ratios is 0.16, and the load phase difference can be approximately equal to the port length ratio. The transmission line lengths of the input and output ports are $\Delta l_1 = 0.5599$ mm and $\Delta l_2 = 0.6158$ mm, respectively. Figure 5 is a comparison diagram of S_{11} and S_{21} after removing the loading phase, respectively. The difference between the red dotted line and the black solid line in the figure reflects the effect of the loading phase on the scattering parameters of the filter.
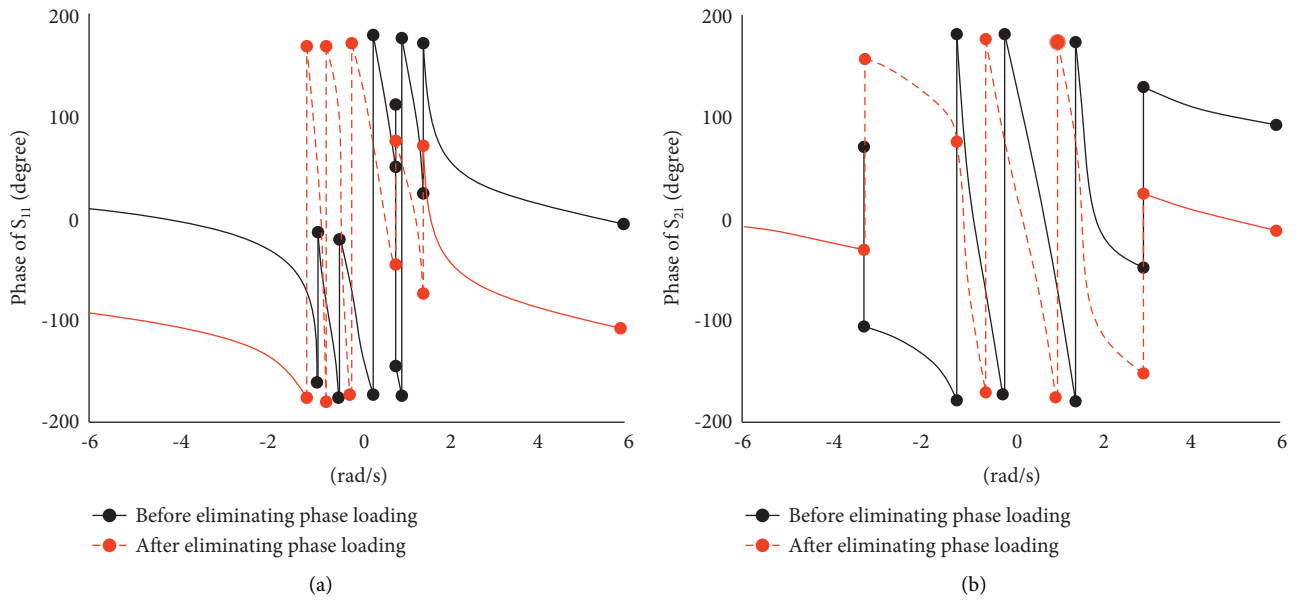
FIGURE 5: Comparison before and after removing the loading phase. (a) Comparison before and after removing the loading phase S_{11}. (b) Comparison before and after removing the loading phase S_{21}.
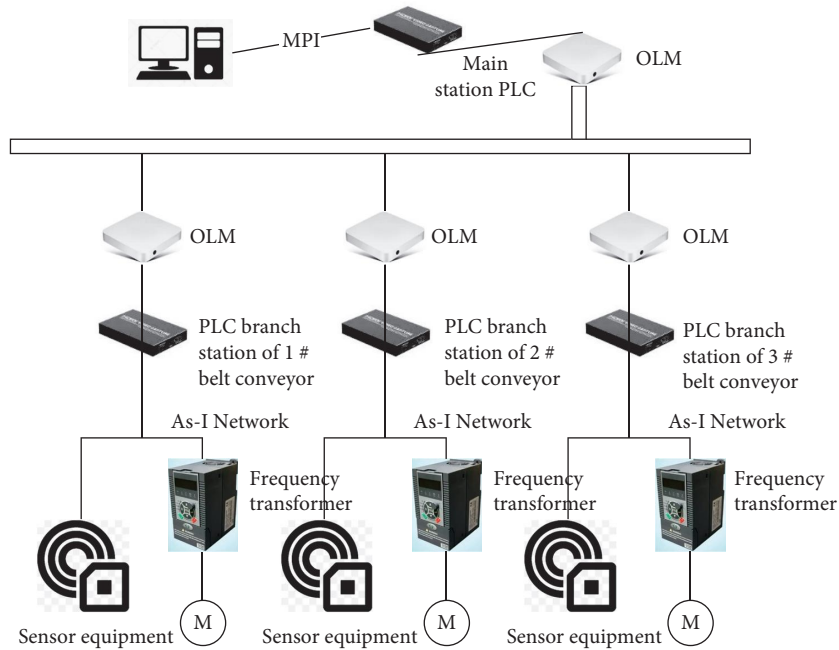

FIGURE 6: System hardware.

3. System Design

The environmental conditions in coal mines are harsh, and the safety performance requirements are extremely high. Therefore, the system hardware should first consider the safety performance of components in harsh environments, and second, it should be able to operate stably for a long time in the well. At the same time, it is necessary to comprehensively consider all aspects to determine the hardware design scheme of the system. System hardware is shown in Figure 6.

The coal mine industrial control network model based on switched industrial Ethernet is adopted, which combines industrial fieldbus/intelligent equipment. The bus mode is used to realize data transmission between the system main controller and sensors, intelligent equipment and emergency stop phones, and industrial Ethernet is used to realize data transmission between the main controller and the ground host. As the key equipment of the whole system, the upward direction of the main controller is to use the industrial Ethernet ring network of the coal mine to realize communication with the system host, and the downward
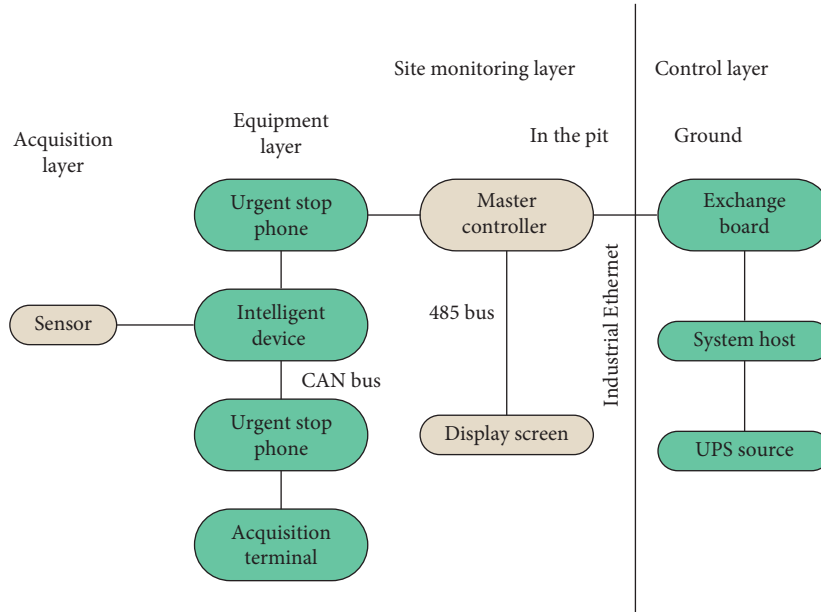
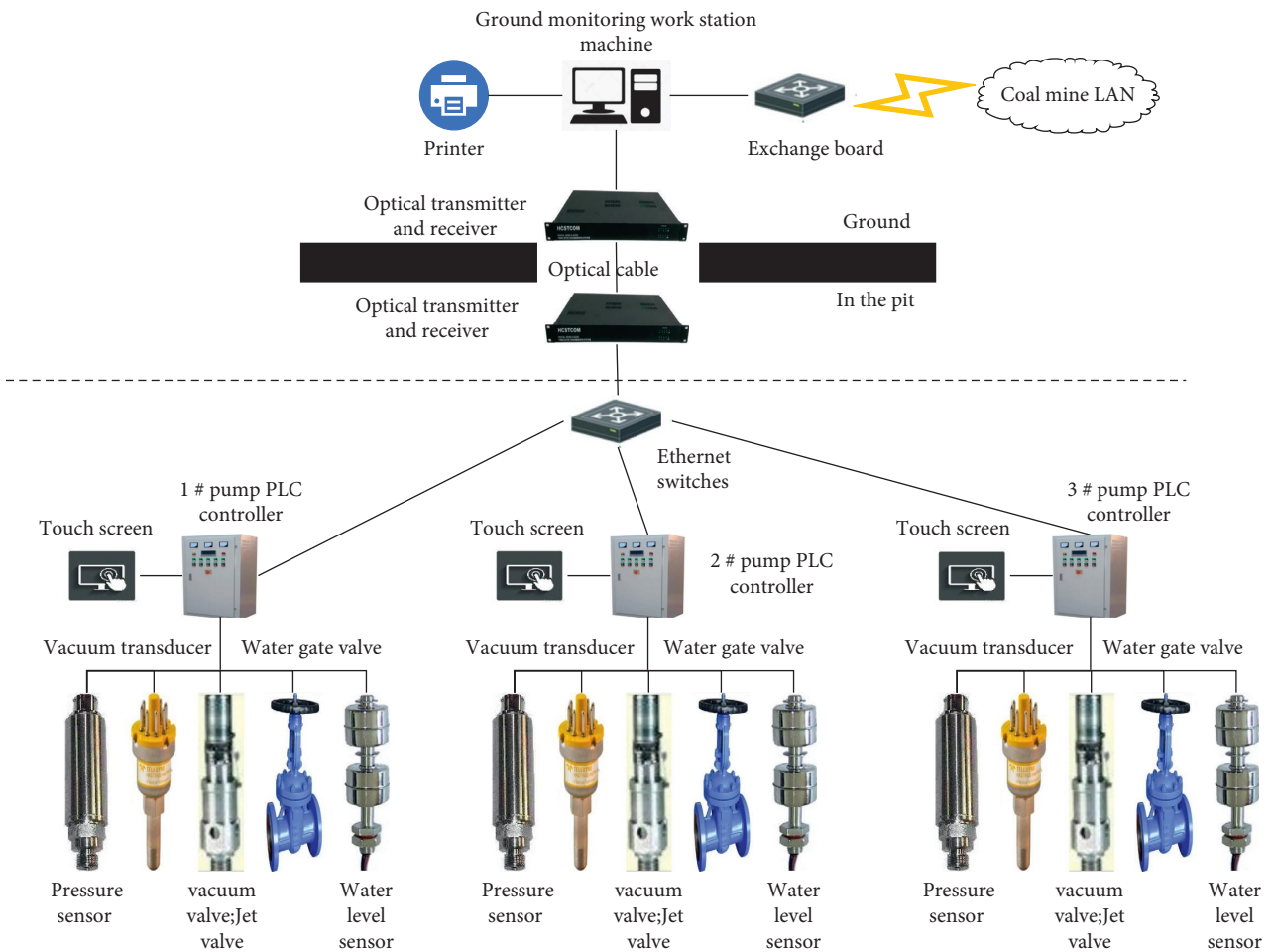FIGURE 7: Transmission system structure.

FIGURE 8: The overall structure of the control system.

TABLE 1: Sensor type and model selection.

Sensor	Working power	Output signal	Temperature range	Measuring distance	Ranging resolution (mm)
Sonic level gauge	DC24 V/AC220 V	Current 0/4 ~ "20 mA, load capacity is less than 600 Q	−20°C ~ 60°C;	0 ~ 25 m;	1
Light sensor	16 V–24 V, current < 24 mA	Current 0/4 ~ 20 mA	700°C ~ 1200°C	0.25 m ~ 20 m	
Ultrasonic flowmeter	AC220 V 50 HZ	Current 0 ~ 20 mA, load capacity is less than 600 Q			
KGY4 negative pressure sensor	DCl8 V, the current is not more than 100 mA	Frequency 200" ~ 1000 Hz, current 4 ~ 20 mA		100 kPa-0 kPa	

direction is to realize the bus communication with the field equipment such as emergency stop telephones, intelligent equipment, sensors, and acquisition terminals along the line. The terminal is responsible for collecting the terminal voltage and the number and location of equipment along the line, and transmitting it to the main controller. The structure of the transmission system is shown in Figure 7.

The control system is mainly composed of PLC control cabinet and host computer, which is the core part of the automatic control system. According to the location, the drainage control system can be divided into ground monitoring upper computer and underground on-site lower computer. The system structure is shown in Figure 8.

(1) The ground monitoring host computer. The ground monitoring system consists of industrial computer, industrial TV system, and optical transceiver. The industrial computer makes the upper computer communicate with the downhole PLC system through the industrial Ethernet. The configuration software is used to build the upper computer, and the underground equipment can be remotely monitored and controlled through the on-site data and dynamic pictures. The operator can remotely control the on-site drainage system through the host computer in the centralized control room, and read the key data of the pump operation in real time, and record and save it. The industrial TV system is used to portray the real-time picture display of the underground pump room, allowing the operator to observe the operation of the pump more conveniently. The connection medium between the ground and the underground is the optical cable, which is connected to the local operation box and the intrinsically safe network camera through the optical fiber junction box, transmits the control signal and video signal to the ground control room, and transmits the underground signal to the Ethernet ring network through the optical transceiver. The host computer realizes the remote centralized control of the system equipment, and controls the motor on and off, valve action and other auxiliary equipment on the host computer. The interface displays

parameters such as water level, outlet pressure, current, etc., and also includes functions such as historical alarm records and external release, so the screen is intuitive and the operation is convenient. (2) Downhole drainage control system. The on-site control system is mainly composed of flameproof PLC control cabinet, intrinsically safe local operation box, sensor, electric (magnetic) gate valve (vacuum valve, jet valve, water outlet gate valve, etc.), high-voltage switch cabinet, and various actuators. In addition, an intrinsically safe network camera is installed in the pump room to monitor the situation of the pump room. The PLC control cabinet is mainly composed of Siemens S7-300 PLC and auxiliary electrical equipment. The PLC part is composed of power supply module, central processing output (CPU), digital input and output module, and analog input and output module. Their function is to collect the return signals and control signals sent by each part of the equipment, and they are responsible for controlling the work of each part. The local operation box is mainly composed of touch screen, optical transceiver, indicator lights and buttons, etc. As a field operation platform, there is a touch screen to display the running status of the water pump. Sensors include flowmeters, water level gauges, vacuum pressure sensors, current transformers, etc., which are used to collect important data on site and participate in control and safety monitoring.

The sensor type and model selection are shown in Table 1.

On this basis, the effect of the automatic control system for the fully mechanized coal mining face constructed in this paper is verified, and the effects of the underground drainage control and transportation control are verified through multiple sets of simulations, and the research results shown in Figure 9 are obtained.

It can be seen from the mentioned research that the automatic control system for fully mechanized coal mining face proposed in this paper has a good intelligent control effect.
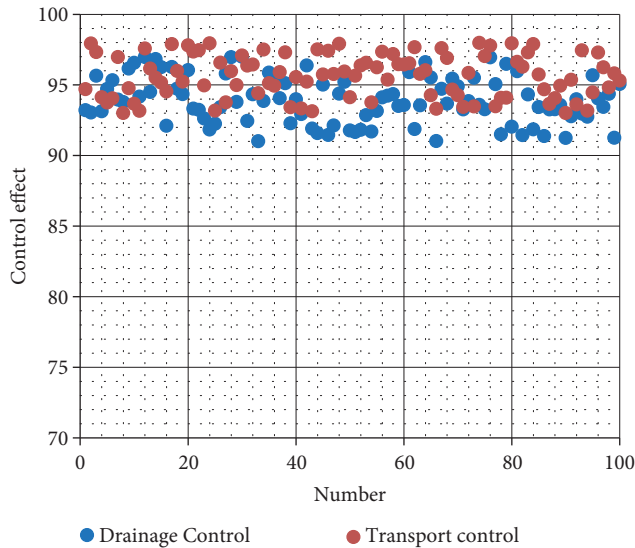
FIGURE 9: Effect verification of automatic control system of fully mechanized mining face in coal mine.

4. Conclusion

In recent years, major coal mining companies have been constantly emphasizing the construction of talent teams and increasing the intensity of talent introduction. The proportion of college students in the company's personnel has increased year by year, and the quality of technical personnel has been greatly improved. Moreover, with the continuous development of the strategy of mechanized replacement and automation of human reduction, mines with a high degree of automation have appeared in the country. However, they still use single-chip technology, preset process flow, poor processing capability, and the number of sensors that can be connected is greatly limited. At the same time, the communication with other systems is based on the bus mode, which cannot be flexibly adjusted according to the actual needs in the later period, and is not conducive to the construction of a comprehensive automation platform for coal mines and hinders the construction of intelligent mines. This paper analyzes the automatic control and performance of the fully mechanized mining face in the coal mine, and constructs an intelligent control system to improve the automatic control effect of the fully mechanized mining face in the coal mine. The experimental research results show that the automatic control system for fully mechanized coal mining face proposed in this paper has a good intelligent control effect.

The follow-up research work of this paper is to expand the object of remote monitoring from the monitoring of the fully mechanized mining face to the monitoring of the inclined shaft transportation system and the belt transportation system, and to establish a system that integrates the functions of information collection, operation control, accident alarm, and auxiliary analysis. The developed coal mine working face and transportation remote monitoring system can remotely transmit the underground working face environmental data, equipment status data, mine pressure data, belt transportation system, and other data to the data center above the mine to realize centralized monitoring of remote data.

Data Availability

The labeled data set used to support the findings of this study is available from the corresponding author upon request.

Conflicts of Interest

The authors declare that there are no conflicts of interest.

References

[1] J. Brodny and M. Tutak, "Applying sensor-based information systems to identify unplanned downtime in mining machinery operation," *Sensors*, vol. 22, no. 6, p. 2127, 2022.

[2] J. Brodny, M. Tutak, and M. Michalak, "The use of the TGŚP module as a database to identify breaks in the work of mining machinery," In *Proceedings of the International Conference: Beyond Databases, Architectures and Structures*, pp. 441–452, Springer, Cham, 2017, May.

[3] J. Wang, G. Zhou, X. Wei, and S. Wang, "Experimental characterization of multi-nozzle atomization interference for dust reduction between hydraulic supports at a fully mechanized coal mining face," *Environmental Science and Pollution Research*, vol. 26, no. 10, pp. 10023–10036, 2019.

[4] H. Peng, W. Nie, P. Cai, Q. Liu, Z. Liu, and S. Yang, "Development of a novel wind-assisted centralized spraying dedusting device for dust suppression in a fully mechanized mining face," *Environmental Science and Pollution Research*, vol. 26, no. 4, pp. 3292–3307, 2019.

[5] G. Zhang, G. Zhou, S. Song, L. Zhang, and B. Sun, "CFD investigation on dust dispersion pollution of down/upwind coal cutting and relevant countermeasures for spraying dustfall in fully mechanized mining face," *Advanced Powder Technology*, vol. 31, no. 8, pp. 3177–3190, 2020.

[6] W. Nie, X. Zhang, H. Peng et al., "Research on air curtain dust control technology for environmental protection at fully mechanized working faces," *Environmental Science and Pollution Research*, vol. 29, no. 28, pp. 43371–43384, 2022.

[7] H. P. Kang, G. F. Wang, P. F. Jiang et al., "Conception for strata control and intelligent mining technology in deep coal mines with depth more than 1000 m," *Journal of China Coal Society*, vol. 43, no. 7, pp. 1789–1800, 2018.

[8] Y. Xie, W. Cheng, H. Yu, and B. Sun, "Microscale dispersion behaviors of dust particles during coal cutting at large-height mining face," *Environmental Science and Pollution Research*, vol. 25, no. 27, pp. 27141–27154, 2018.

[9] X. Zhang, P. Gong, K. Wang, J. Li, and Y. Jiang, "Characteristic and mechanism of roof fracture ahead of the face in an LTCC panel when passing an abandoned roadway: a case study from the Shenghua coal mine, China," *Rock Mechanics and Rock Engineering*, vol. 52, no. 8, pp. 2775–2788, 2019.

[10] H. Shi, J. Xie, X. Wang, J. Li, and X. Ge, "An operation optimization method of a fully mechanized coal mining face based on semi-physical virtual simulation," *International Journal of Coal Science & Technology*, vol. 7, no. 1, pp. 147–163, 2020.

[11] X. Liu, D. Fan, Y. Tan et al., "New detecting method on the connecting fractured zone above the coal face and a case study," *Rock Mechanics and Rock Engineering*, vol. 54, no. 8, pp. 4379–4391, 2021.

[12] D. Wei, Z. Wang, L. Si, C. Tan, and X. Lu, "Online shearer-onboard personnel detection method for the intelligent fully mechanized mining face," *Proceedings of the Institution of*

Mechanical Engineers - Part C: Journal of Mechanical Engineering Science, vol. 236, no. 6, pp. 3058–3072, 2022.

[13] X. Yang, G. Wen, L. Dai, H. Sun, and X. Li, "Ground subsidence and surface cracks evolution from shallow-buried close-distance multi-seam mining: a case study in Bulianta coal mine," *Rock Mechanics and Rock Engineering*, vol. 52, no. 8, pp. 2835–2852, 2019.

[14] X. Shi, H. Jing, J. Ning, Z. Zhao, and J. Zhu, "Stability control of gob-side entry retaining in fully mechanized caving face based on a compatible deformation model," *Computer Modeling in Engineering and Sciences*, vol. 124, no. 1, pp. 315–343, 2020.

[15] P. Zhao, R. Zhuo, S. Li, C. H. Ho, H. Lin, and H. Liu, "Research on the effect of coal seam inclination on gas migration channels at fully mechanized coal mining face," *Arabian Journal of Geosciences*, vol. 12, no. 18, pp. 597–614, 2019.

[16] L. Fan and X. Ma, "A review on investigation of water-preserved coal mining in western China," *International Journal of Coal Science & Technology*, vol. 5, no. 4, pp. 411–416, 2018.

[17] D. Z. Kong, Z. B. Cheng, and S. S. Zheng, "Study on the failure mechanism and stability control measures in a large-cutting-height coal mining face with a deep-buried seam," *Bulletin of Engineering Geology and the Environment*, vol. 78, no. 8, pp. 6143–6157, 2019.

[18] B. Li, Y. Liang, and Q. Zou, "Determination of working resistance based on movement type of the first subordinate key stratum in a fully mechanized face with large mining height," *Energy Science & Engineering*, vol. 7, no. 3, pp. 777–798, 2019.

[19] H. Wang, W. Cheng, B. Sun, H. Yu, and H. Jin, "The impacts of the axial-to-radial airflow quantity ratio and suction distance on air curtain dust control in a fully mechanized coal face," *Environmental Science and Pollution Research*, vol. 25, no. 8, pp. 7808–7822, 2018.